



## City Research Online

### City, University of London Institutional Repository

---

**Citation:** Rahman, E., Liatsis, P., Hashim, Z. Q., Kyriacou, P. A. & Triantis, I. F. (2024). A Quadruple-Sweep Bioimpedance Sensing Method for Arterial Stenosis Detection. *IEEE Access*, 12, pp. 18594-18605. doi: 10.1109/access.2024.3356564

This is the published version of the paper.

This version of the publication may differ from the final published version.

---

**Permanent repository link:** <https://openaccess.city.ac.uk/id/eprint/32107/>

**Link to published version:** <https://doi.org/10.1109/access.2024.3356564>

**Copyright:** City Research Online aims to make research outputs of City, University of London available to a wider audience. Copyright and Moral Rights remain with the author(s) and/or copyright holders. URLs from City Research Online may be freely distributed and linked to.

**Reuse:** Copies of full items can be used for personal research or study, educational, or not-for-profit purposes without prior permission or charge. Provided that the authors, title and full bibliographic details are credited, a hyperlink and/or URL is given for the original metadata page and the content is not changed in any way.

---

---

---

City Research Online:

<http://openaccess.city.ac.uk/>

[publications@city.ac.uk](mailto:publications@city.ac.uk)

---

Date of publication xxxx 00, 0000, date of current version xxxx 00, 0000.

Digital Object Identifier 10.1109/ACCESS.2017.DOI

# A Quadruple-Sweep Bioimpedance Sensing Method for Arterial Stenosis Detection

ENAYETUR RAHMAN<sup>1</sup>, PANOS LIATISIS<sup>2</sup>, (Senior Member, IEEE), ZAHEER Q. HASHIM<sup>1</sup>, (Student Member, IEEE), PANAYIOTIS A. KYRIACOU<sup>1</sup>, (Senior Member, IEEE), AND IASONAS F. TRIANTIS.<sup>1</sup>, (Senior Member, IEEE)

<sup>1</sup>E. Rahman, Z. Hashim, P. Kyriacou and I. Triantis are with the Research Centre for Biomedical Engineering (RCBE), City, University of London, London, UK, e-mail: {enayet.rahman.2, zaheer.hashim, p.kyriacou, i.triantis}@city.ac.uk

<sup>2</sup>P. Liatsis is with the Department of Electrical Engineering and Computer Science, Khalifa University of Science and Technology, Abu Dhabi, UAE, e-mail: panos.liatsis@ku.ac.ae

Corresponding author: Iasonas F. Triantis (e-mail: i.triantis@city.ac.uk).

**ABSTRACT** Current carotid atherosclerosis diagnostic protocols do not feature techniques that would allow for early or frequent medical examinations, leaving a significant number of asymptomatic carotid stenosis cases undetected and often leading to strokes. The key challenge is that current diagnostics are highly operator-dependent. In this work we used idealised biological models to demonstrate a new rapid, potentially inexpensive and operator-independent diagnostic method, aimed at detecting whether a stenosis exists, rather than seeking to be accurately quantifying or localising it. An array of electrodes was used to obtain sequential bioimpedance values over the skin, through a novel scanning technique, covering an area over the artery of interest. FEM simulations, verified through in-vitro experiments on gelatine phantoms, were used to validate the method. The final results, obtained through image processing algorithms, were in the form of planar bio-impedance maps and were successful both in identifying arterial features and detecting the presence of stenoses of different sizes. The results could also be used to indicate the artery's relative orientation to the sensor, eliminating the need for manual alignment by a specialist operator. Therefore, this method shows promise for routine medical examination, either in primary care, or even at home, to indicate whether a patient would require further, more detailed examinations at a specialist clinic.

**INDEX TERMS** Bioimpedance sensing, Cardiovascular Diagnostics, Carotid artery screening, FEM modelling, Image processing, Impedance scanning, Planar bioimpedance mapping, Stenosis detection

## I. INTRODUCTION

CAROTID artery disease can have devastating consequences, as it is one of the main causes of stroke. Stroke affects 15 million people around the world annually, with more than 60% of all cases caused by carotid atherosclerosis, 80% of which are asymptomatic [1], [2]. The resulting arterial stenosis or occlusion can become symptomatic in people over 40 years of age, while asymptomatic stenosis may occur at an earlier age [3].

To date, ultrasound imaging [4] is the gold standard for non-invasive detection of carotid artery stenosis once symptoms appear, referring positive outcomes for further tests based on CT or MRI scans. The method is almost always used by means of a hand-held probe, which is moved and rotated by a specialised operator, visualising the structure of

interest from different angles [5] (Fig. 1(a)). However, the quality and reliability of the outcome strongly depends on the expertise of the person handling the probe, making the process highly operator-dependent. This results in up to 18% of the diagnoses being erroneous, either as false positives or false negatives [1], [6]. This operator dependency coupled with the cost of a full ultrasound imaging system makes the technique suitable for use predominantly in specialist clinics [7], being carried out only when clear symptoms occur [1], which is often too late. More importantly, these issues preclude ultrasound carotid scanning from being part of routine medical checks. As a result, for the asymptomatic majority of patients [1], such a scan will not take place at all before a potentially life changing or fatal stroke occurs.

In order to carry out regular carotid screening tests to

every person meeting certain criteria (e.g., age, diet), it is desirable to have a low cost, operator-independent, non-invasive method to provide an indication of arterial stenosis or occlusion without waiting for symptoms to occur. Such a method would not aim at replacing ultrasound, but rather it would allow for suspected cases to be referred for ultrasound examination and subsequent further tests, if needed. It would ideally be available in primary care, as well as low resourced healthcare settings and even for home use. Enabling routine tests on all patients that visit a doctor could potentially allow for preventive action for a great number of stroke sufferers annually [1].

Acknowledging these issues with conventional ultrasound apparatus, recent research studies have presented attempts towards more portable, even wearable, ultrasound devices [8], [9]. Still these devices require a specialist operator to achieve orthogonal (perpendicular or parallel) placement relative to the underlying artery and they are relatively cumbersome and thus sensitive to movement and potentially obstructive to the patient. A sensing modality that would allow for a point-of-care (PoC) diagnostic device to satisfy the above criteria is bio-impedance (or electrical impedance). Bioimpedance has been used in a variety of medical applications, ranging from cardiovascular plethysmographic measurements [10]–[13], lung monitoring [14], [15], detection of breast cancer [16], mapping wound areas in chronic ulcers [17] and many others [18], [19]. Bioimpedance systems are inexpensive, easy to use without specialist training, providing rapid outcomes without the use of harmful ionising radiation [10]. While measurements can be prone to errors due to the surface electrochemistry of the electrodes used, this can be overcome through the use of tetrapolar (four-electrode) configurations [20]. In a tetrapolar setup, measurements are carried out by applying a small amplitude alternating current using a pair of electrodes placed on the skin and then measuring the resulting potential using a second pair of electrodes [19]. Recent studies have shown that it is possible to detect atherosclerotic plaques through tetrapolar bioimpedance measurements [21], making this sensing modality a possible candidate for early detection of carotid stenosis.

However, single tetrapole arrangements ideally need to be aligned to the targeted artery, thus requiring the latter's location and orientation to be known in advance. Failing to place and size the electrodes accordingly, degrades measurement sensitivity due to the surrounding tissue's impedance [13]. Moreover, the approach of analysing plethysmographic waveform features for indications of stenosis presence, while valuable, does not reveal any topological information. Such information can typically be offered by imaging, with electrical impedance tomography (EIT) [20] meeting several of the above criteria. However, the method is too cumbersome, complicated and expensive for routine medical examinations as, in its most portable embodiment, it requires an electronic setup similar to a "tower" desktop computer on wheels, making it unsuitable for the majority of primary care practices, remote areas, or home use [22], [23]. Additionally, for EIT-

based carotid artery scanning, electrodes would need to be applied around the neck of the patient and, given its poor spatial resolution [18], [19], [24], it would not offer useful information about a localised structure, such as the carotid artery. Solutions that include elements from both the single tetrapole and the EIT approaches have been described in [13], [25]. For the desired method, topological information is needed to detect the outline of the artery, in terms of position and orientation, to avoid the operator dependence of manually re-positioning the sensor. While the presence of features, such as arterial bifurcations and possible stenoses, need to be detected in order to generate an indicative diagnostic outcome, there is no need at a routine screening test to extract a detailed image involving elaborate hardware, algorithms and forward models.

The work presented here proposes and assesses a multi-electrode sensing method using bioimpedance measurements to provide what we introduce as localised planar bioimpedance mapping (PBiM) of transcutaneous vascular features. A possible neck-worn realisation is shown in Fig. 1(b), along with the methodological steps followed in this research. While - in a similar fashion to EIT - we use imaging techniques to extract the aforementioned data, there is no requirement to use a forward model or computationally demanding reconstruction algorithms.

More specifically, in this work an electrode array is used to carry out a novel bioimpedance scanning sequence, both by using finite element modelling (FEM) simulations and experimentally on gelatine phantoms, to detect non-invasively the position and orientation of a blood vessel underneath the skin, thus eliminating the need for sensor alignment that would require a specialised operator. The associated bioimpedance images are processed for blood vessel features, including bifurcations and, in particular, the presence of stenosis.

This work builds on our previous work, described in [13] and [25]. In [13] we identified the advantage of localised electrodes, placed directly above the targeted subcutaneous vasculature, relative to larger more commonly used electrodes (e.g. ECG electrodes). In [25] we presented an array and a unidirectional scanning approach and we separately identified the advantages of localised electrodes. Here we expand on these concepts, using a planar array as a potential non-operator dependent imaging tool with a newly introduced quadruple sweep scanning approach, analysing the sensor's operational principles, and highlighting its strengths in terms of spatial resolution and in detecting arteries of different angles and bifurcations.

The novelty of this approach lies in the aforementioned properties, which allow for portability and minimal operator dependency. To the best of the authors' knowledge, there is no state-of-the-art solution for planar mapping of the carotid artery. PBiM utilises tetrapolar bioimpedance interfacing. It features further innovative aspects in the methodology, as it interrogates tissue through tetrapoles of fixed inter-electrode distance, as opposed to EIT, where the tetrapole dimensions

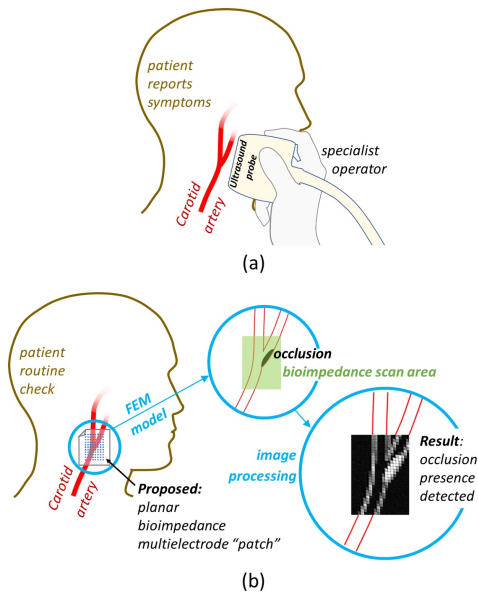


FIGURE 1: Carotid artery scanning using: (a) A standard ultrasound probe. (b) The proposed - operator independent - planar bioimpedance mapping method.

vary. In this manner, the measurements are directly comparable without the need for a forward model. Moreover, given the fact that a tetrapole provides measurements over the underlying tissue volume rather than point measurements at the tetrapole centre [19], we introduced a novel scanning method, whereby an area is swept four times in each of four different directions (i.e., Vertical, Horizontal, Diagonal-right and Diagonal-left) automatically through electrode-addressing instrumentation. The four resulting images, or bio-impedance "planar maps", are combined so as to achieve higher spatial resolution and less dependency on the underlying blood vessel's orientation. A COMSOL model with simplified biological features [26], [27], [28] was used to assess the method, while experimental verification was performed on a smaller physical model (gelatine phantom).

In section II, the procedure for setting up the simulation and performing the experimental studies with four variants of a biological model and a multi-electrode array is discussed. In particular, the parameters, i.e., vessel orientation, bifurcation angles and percentage stenosis, used to assess the performance of the method, are described. Section III presents and discusses the results obtained from the application of the method. Finally, section IV presents the conclusions and avenues for further work.

## II. METHOD

A three-dimensional biological model was designed to calculate electrical impedance sensed by electrodes placed on the top surface, representing the skin. Aiming to explore the principles and merits of planar mapping and similar to other studies (e.g. [13]) this model was simplified in terms of its composition and its geometrical complexity, as it was limited

to three homogeneous tissue layers (see section II-A) without any other vasculature in the vicinity. Two versions were realised, as described later: an FEM model and a gelatine phantom for experimental verification. An array of electrodes was used with the active tetrapole being dynamically reconfigurable in terms of position and orientation, in resemblance to [13], modelled to assess local impedance variations corresponding to vascular structures underneath the skin. The first objective was to check whether it is possible to detect the presence of a blood vessel and subsequently, to detect its orientation, towards the goal of making the method operator-independent by eliminating the need of manually aligning the sensor to the vessel. The next objective was to assess the possibility of detecting the presence of a stenosis within the blood vessel from the electrical impedance scan. Blood vessels with and without stenoses were studied, both of straight-line and bifurcated shapes. The latter was included to represent the most usual region of atherosclerotic plaque build-up in the carotid artery, at the bifurcation between the external and internal carotid arteries. A reduced-size version of the model with a straight-line vessel was experimentally verified. In all cases, the 2D impedance map obtained from each scan was processed with advanced image processing algorithms to automate the detection of the various features of interest.

### A. FEM MODEL

The objectives of the simulations were: a) To construct a simplified biological model (similar to [13]) including the tissue layers that contribute the majority of the sensed impedance values (i.e., skin, fat) and a blood vessel representing the carotid artery. b) To model scenarios that represent relatively random placement of the electrode array over the blood vessel through variations in their relative orientation and slight shifts in their relative position. c) To model arterial features, such as bifurcations, and the occurrence of atherosclerosis, i.e., stenosis through local plaque buildup. d) To perform sweeps or "scans" of impedance measurements by moving fixed-size electrode tetrapoles in four different directions, using an electrode array placed over the blood vessel.

The simulations were carried out using the COMSOL 5.3 electric currents (ec) module, where the quasi-static solutions of Maxwell's equations were used to solve for the electrical potential. The electrodes placed on the top surface were used as current injection or recording terminals. As biocompatibility and electrode corrosion are issues in simulation, the simulated injection current was kept at 1A for simplicity. Adaptive physics controlled meshing at the finer setting was used, where the mesh density was kept very high at locations of interest, i.e. the vascular features.

A cuboid shape model was considered with two layers, a 2 mm thick skin layer and an 8 mm thick fat layer, where the carotid artery was considered to be in the fat layer (Fig. 2(a)) and the anatomical properties of the model were kept consistent with [29], [30]. The typical depth of the carotid artery in the neck from the outer skin layer is  $(6 \pm 3)$  mm

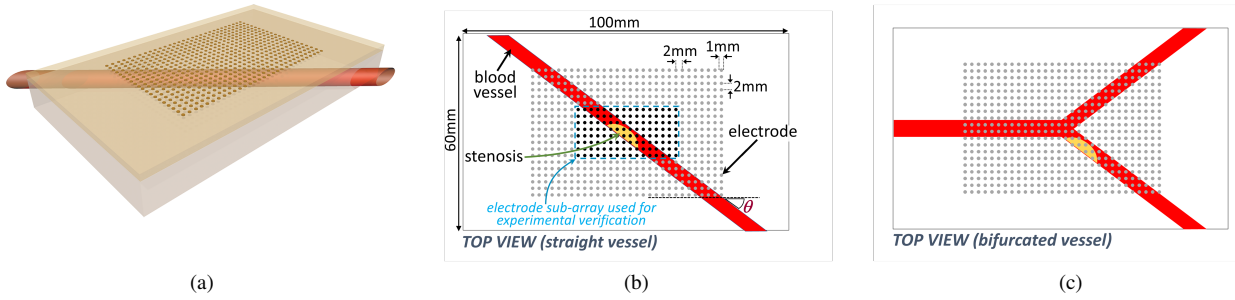


FIGURE 2: Overview of the biological model with the  $20 \times 30$  electrode array used for the FEM simulations on top: (a) 3D COMSOL model. (b) Top view of the  $-37^\circ$  straight artery model with stenosis shown as a yellow region in the straight vessel. The smaller group of dark-coloured electrodes in the middle of the main array represent the  $8 \times 16$  sub-array used for the experimental verification. (c) Top view of the bifurcated artery model with stenosis shown as a yellow region in one branch of the bifurcation.

[31], and in the model the depth was taken as  $7 \text{ mm}$ . For the sake of model simplicity, it was assumed that the carotid artery is embedded in a fat layer underneath the skin and no muscle tissue is present between the skin and the arterial wall. It was also assumed that all media are homogeneous and that the top surface of the skin is flat. The conductivity and relative permittivity values assigned to the skin, fat and blood layers were obtained from [32], [33].

Specifically, the conductivity values for skin, fat and blood were set to  $2.937 \text{ mS/m}$ ,  $42.954 \text{ mS/m}$  and  $700.04 \text{ mS/m}$ , respectively, while the relative permittivity values were set to 29010, 911.54 and 5248.2 respectively, at a frequency of 10KHz, calculated using Eq.(1) [33], [34]:

$$\hat{\epsilon}(\omega) = \epsilon_\infty + \sum_{m=1}^4 \frac{\Delta\epsilon_m}{1 + (j\omega\tau_m)^{(1-\alpha_m)}} + \frac{\sigma_i}{j\omega\epsilon_0} \quad (1)$$

In the above equation  $\hat{\epsilon}(\omega)$  is the complex relative permittivity as a function of frequency,  $\epsilon_\infty$  is the permittivity at frequencies, where  $\omega\tau \gg 1$ , and  $\tau$  represents a time constant. The magnitude of the dispersion is given as  $\Delta\epsilon_m$ ,  $\sigma_i$  is the static ionic conductivity and  $\epsilon_0$  is the permittivity of free space. The distribution parameter,  $\alpha$ , is a measure of the broadening of the dispersion.

Atherosclerotic plaques within the blood vessel comprise fat deposits and calcium hydroxyapatite (CHA, commonly referred to as pathological calcification), which can make up to a maximum of 30% of the total stenosis [35]. Therefore, the conductivity and relative permittivity of fat [33] and those of CHA at room temperature [36] at 10kHz were taken and combined in the ratio of 70 : 30 to obtain the electrical properties of the stenosis to be used in our simulations. Considering this, the conductivity and relative permittivity of the stenosis were set to  $1.4 \text{ (mS/m)}$  and 280, respectively.

The dimensions of the COMSOL model were  $100 \text{ mm} \times 60 \text{ mm} \times 10 \text{ mm}$  with a  $2 \text{ mm}$  thick skin layer at the top and an  $8 \text{ mm}$  fat layer underneath the skin. The blood vessel was placed in the fat layer with its centre  $7 \text{ mm}$  below the

top surface of the skin. By changing various parameters, it was possible to change the location, orientation and diameter of the blood vessel. Both straight (Fig. 2(b)) and bifurcated (Fig. 2(c)) blood vessels were considered. It was also possible to vary the size and the location of an atherosclerotic plaque stenosis within a blood vessel. The stenosis was modelled as an ellipsoid with radii of  $r_{length} \times r_{width} \times r_{height}$ . Using the top view of the model (Fig. 2(b)), its centre was placed on the vessel-fat boundary at the middle of the blood vessel's length on the side facing the bottom left of the electrode array. The depth of its centre was  $7 \text{ mm}$  and its length  $r_{length}$  was  $6 \text{ mm}$ , parallel to the vessel's longitudinal axis. Its height  $r_{height} = 3 \text{ mm}$  was vertical to the electrode plane. Its radius along its width was  $r_{width} = D_{bv} \times X_{occ}$ , where  $D_{bv}$  is the diameter of the vessel in mm and  $X_{occ}$  is the stenosis size as a percentage of the vessel diameter.

In the simulation, the top surface was considered as the xy plane and the depth was along the z axis. All parameter variations in this study can be categorised into the following four test cases:

- **Case I:** Straight vessel without stenosis. Parameter variations: Orientation =  $\{0^\circ, -15^\circ, -37^\circ, -45^\circ, -90^\circ\}$ . For each of the orientations, the simulation was carried out for five slightly different variants in the vessel's position, in order to test whether the scanning method and the image processing algorithm could still detect the vessel with some degree of randomness added to the blood vessel parameters. The five (x,y) position coordinates of the vessel's centre in relation to the initial central position were  $(-2 \text{ mm}, 0)$ ,  $(0, 0)$ ,  $(2 \text{ mm}, 0)$ ,  $(0, -2 \text{ mm})$  and  $(0, 2 \text{ mm})$ , with the vessel's diameter fixed at  $5 \text{ mm}$ . Subsequently, with the vessel at its original position, four different diameters were considered with values of  $\{5.5 \text{ mm}, 6 \text{ mm}, 6.5 \text{ mm}, 7 \text{ mm}\}$  resulting in a total of 45 simulations.
- **Case II:** Straight vessel with stenosis. The percentages of stenosis were  $\{0\%, 20\%, 40\%, 60\%$ ,

80%}. For each of the stenoses, the same nine total variations in the vessel's location and diameter as in case I were considered, while keeping the vessel orientation at  $-37^\circ$ . A total of 45 simulations were considered.

- **Case III:** Bifurcated vessel without stenosis. Again, as in case I, five variations of location and four variations of diameter were considered, keeping the orientation of the main vessel at  $0^\circ$  and the angle between the bifurcated vessels at  $73^\circ$ , bringing the total number of simulations to 9.
- **Case IV:** Bifurcated vessel with stenosis. Five variations of stenosis, i.e., {0%, 20%, 40%, 60%, 80%} were simulated. For each of the stenoses, five variations of the blood vessel's location, and four variations of its diameter were considered, while keeping the orientation of the main vessel at  $0^\circ$  and the angle between the bifurcated vessels at  $73^\circ$ , resulting in 45 simulations.

### B. SIMULATION SCANNING SEQUENCE

All simulations featured "shifting" tetrapoles formed by in-line neighbouring electrodes, with the outer pair always being the current-carrying (CC) electrodes, and the inner pair assigned the voltage pick-up (PU) function. One of the CC electrodes was modelled as a current terminal with a boundary condition of 1 A, while the other was modelled as a ground terminal of a zero potential. It was assumed that no current flows through the exterior boundaries of the phantom, modelled as air. The two PU electrodes were modelled as boundary probes, from which the resulting potentials were measured. The transfer impedance was then obtained by dividing the difference of the voltage values at the two boundary probes by the applied current. A  $20 \times 30$  electrode array was used in the FEM simulations (Fig. 2). The overall array size must be kept as small as possible for practical reasons and in order to span over a limited scanning area and thus the inter-electrode distance should be kept to a minimum. Studies such as [37] and [38] have indicated that the depth of penetration of the bioelectric field is predominantly influenced by the inter-electrode separation. Although, in theory, the electric fields can extend to infinite depth, for the practical purpose of impedance measurements, detection accuracy diminishes significantly beyond a depth of 4-5 times the inter-electrode distance. Initial simulations for the model dimensions of this paper indicated that measurement sensitivity for inter-electrode distances smaller than 2 mm is inadequate for vessel detection while it plateaus for distances larger than 5 mm. Therefore, the minimum acceptable inter-electrode distance is 2 mm, which is the value that was used here, and for which a maximum penetration depth of 10 mm is possible for this inter-electrode distance. For structures located deeper, we have to adjust the inter-electrode distance. For similar reasons, the electrode should be kept at a minimum. The chosen size here was 1 mm as smaller sizes would contribute higher thermal noise [39], [40] and electrode-electrolyte contact impedance. These parameters play no role

in this paper, however in an experimental implementation they would affect both the current injection and the voltage measurement instrumentation.

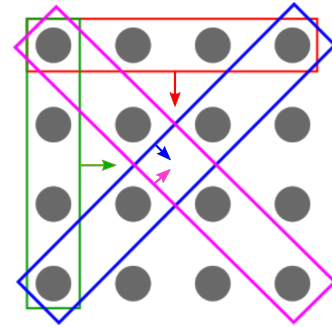


FIGURE 3: Four directional scanning. The vertical, horizontal, diagonal left and diagonal right scanning sequences are indicated in green, red, blue and magenta outlines and arrows, respectively.

Fig 3 illustrates a  $4 \times 4$  segment of the full array to visualise the four scanning sequence orientations, i.e., vertical, horizontal, diagonal left, and diagonal right scans.

The *vertical scan* (red outline in Fig. 3) started with the first four horizontal electrodes of the array. After obtaining the transfer impedance, the tetrapole was shifted by one row at a time until the last row, before shifting by one column and repeating the sequence until the bottom right four electrodes in the last row were reached. In a similar fashion, rotated by  $90^\circ$ , the *horizontal scan* (green outline in Fig. 3) started with the left-top vertical tetrapole, shifting to the right, until eventually reaching the bottom four electrodes of the rightmost column of the array. Each of the *diagonal left* and *diagonal right* scans (blue and magenta outlines respectively in Fig. 3) started with first possible forward slash and backslash diagonal tetrapoles at the upper left and upper right corners respectively. As in the previous scans, the transfer impedance was obtained for all similar tetrapoles in the array.

The four scanning sequences were used in all simulation steps, using the full  $20 \times 30$  electrode array. For each step, the resulting impedance values of the overlapping areas covered in the four respective directions were used to calculate the overall impedance of the underlying volume of that area, as described in section II-D.

### C. EXPERIMENTAL VERIFICATION

The experimental part of the work was carried out to validate the simulation outcomes. One of the straight vessel orientations of Case I, namely  $-37^\circ$ , was replicated in gelatine. Generating a more sophisticated system beyond expanding the slightly the one presented in [13] was beyond the scope of this work and thus due to circuit complexity constraints it was deemed adequate to confirm the simulation findings using a smaller array and a smaller phantom. Therefore a downsized version of the model was simulated and a matching experimental model was generated. They both used a

smaller  $8 \times 16$  electrode array (termed elsewhere in this text as the "sub-array") which was just enough to achieve a vessel orientation identification and thus to allow for a comparison of simulations and experiments. Six identical phantoms were constructed with dimensions  $30 \text{ mm} \times 50 \text{ mm} \times 10 \text{ mm}$  using gelatine (Fig. 4) with multiple layers with a range of conductivities [41], [42]. The phantom layers and shape, including the straight blood vessel at an angle of  $-37^\circ$ , were formed by sequentially pouring and cooling gelatine in 3D printed moulds.

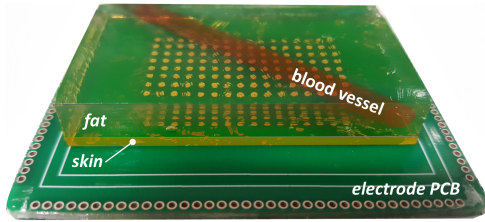


FIGURE 4: Gelatine phantom used in experiments with different layers designated, placed face-down on the electrode array PCB.

Tissue conductivities were calculated at 10KHz using Eq. (1) and values taken from [33]. The conductivities of the corresponding phantom layers were matched to those of the respective biological tissues at 10KHz, by calculating the required NaCl concentrations through Eq. (2) and according to the work in [42], similar to the work in [41]–[43]:

$$\sigma = 200 \times \frac{M_{NaCl}}{V_{Solution}} \quad (2)$$

where  $\sigma$  ( $S/m$ ) is the target conductivity of the layer in  $S/m$ ,  $M_{NaCl}$  is the mass of required NaCl in grams and  $V_{Solution}$  is the volume of the solution in  $ml$ .

Table 1 lists the resulting NaCl concentrations used for making the gelatine phantom layers. A PCB with a planar

TABLE 1: NaCl Concentration of the phantom layers

Layer	Layer Conductivity ( $S/m$ )	Layer NaCl Concentration ( $g/100 \text{ ml}$ )
Skin	0.003	0.0014
Fat	0.043	0.02
Blood	0.70004	0.325

electrode array with  $8 \times 16$  electrodes was fabricated to experimentally verify the results obtained from a simulation model with identical dimensions. The PCB electrodes were disk-shaped with the same diameter and spacing as in the simulations. Using instrumentation as in [13], a Keysight E4980A impedance analyzer was used to obtain the transfer impedance from each tetrapole, following the same scanning sequence as in the simulation studies, described in section II-B. The analyzer was configured to give real and imaginary (R & I) values at 10kHz. The impedance analyser features four terminals, which are labeled  $L_{cur}$ ,  $H_{cur}$ ,  $L_{pot}$  and  $H_{pot}$ .

The  $L_{cur}$  and  $H_{cur}$  terminals are used to inject current and were connected to the CC electrodes. The  $L_{pot}$  and  $H_{pot}$  terminals are used to measure potential and were connected to the PU electrodes.

#### D. IMAGE PROCESSING FOR VESSEL FEATURE ESTIMATION

The objectives of the image processing were: a) to combine, for each of the cases, the data from the four individual scans in one 2D impedance map so as to detect the vessel, if this is located under the electrode array; b) to calculate vessel orientation relative to the array; c) to perform the identification of features, including vessel boundaries and bifurcation using image processing methods; and d) to detect the occurrence of vessel stenosis using appropriate information.

The data obtained with the scanning procedure set out in section II-B correspond to horizontal ( $0^\circ$ ), vertical ( $90^\circ$ ) and diagonal ( $45^\circ$  and  $135^\circ$ ) scanning directions. For all models using  $m \times n$  electrodes (including the smaller sub-array used in experimental verification), these resulted in arrays with respective sizes of  $m \times (n - 3)$  for the vertical scan,  $(m - 3) \times n$  for the horizontal scan and  $(m - 3) \times (n - 3)$  for each for the two diagonal scans. In order to produce a composite image, which combines the information from each of the scans, the impedance measurement of each tetrapole was allocated to the  $(x, y)$  coordinates of the corresponding two PUF electrodes on the top surface of the volume. In order to reduce the effect of measurement noise, distance-based weighted averaging was then performed, taking into account the scanning orientation. The Euclidean distance was used in the experiments, with the corresponding weights being proportional to 1 for the horizontal/vertical matrices, and  $\sqrt{2}$  for the diagonal ones, respectively. The result of this process, which combined together the measurement data from the four scanning directions, is an array of size  $(m - 2) \times (n - 2)$ .

The image processing steps were as follows:

- Thresholding was applied to separate the vessel from background tissues using Otsu's method [44]. The concept of Otsu's approach is to find the threshold value that maximizes the between-class variance of the image histogram, which is a measure of the separation between the two classes of the image pixels, i.e., background and vessel. This method has several advantages including simplicity, speed, and the ability to handle images with varying contrast and lighting conditions.
- The vessel boundaries were detected using the mathematical operator of closing [45]. This is a combination of the erosion and dilation operators. Firstly, erosion is applied to remove small noisy objects and smooth out the boundaries of the vessel. Next, dilation is applied to fill in gaps in the vessel boundaries and restore the size of the vessel region. Following this, thinning [46] is applied, thus resulting in single-pixel width vessel boundaries.
- In order to detect the presence of bifurcations, skeletonization [46] was applied to the binary vessel region,

obtained in step (a). The number of neighbours,  $N_{skel}$  of the electrodes belonging to the skeleton of the vessel was calculated and used to classify them as follows:

$$N_{skel} = \begin{cases} 1, & \text{electrode is an endpoint} \\ 2, & \text{electrode is part of the skeleton} \\ \text{otherwise,} & \text{electrode indicates the location of a bifurcation} \end{cases}$$

This produced a list of candidate bifurcation points along the skeleton of the vessel object, which could then be used to segment it into main vessel and side branches.

- (d) Identification of the parts of the object, which belong to the main vessel and side branches was performed by finding the intersection points of the normal vectors on either side of the bifurcation and the end points belonging to the skeleton of the vessel, using the vessel boundaries detected in step (b).
- (e) The orientation of each segment of the vessel object was estimated by averaging the orientations of the left and right vessel boundaries. Boundary orientation was determined by calculating the least squares estimates of the best fitting straight line to the boundary pixels.
- (f) The bifurcation angle was estimated by subtracting the orientations of the two vessel branches, obtained in step (e).
- (g) To detect the presence of stenosis in a vessel, the k-means++ method was used. k-means clustering is a popular clustering approach, which partitions data into k clusters based on their similarity. However, it is sensitive to the initial centroid selection and tends to converge to local optima. Arthur and Vassilvitskii [47] proposed the k-means++ method which selects the initial centroids in a way that reduces the changes of convergence to a poor local optima. The basic steps of the methods are as follows:
  - a) Initialization: The first centroid is randomly chosen from the data points.
  - b) Iterate over the remaining k-1 centroids:
    - i) For each data point, compute the squared distance between the data point and the nearest centroid that has been already chosen;
    - ii) Select the next centroid randomly, with probability proportional to the squared distance computed in the previous step.
  - c) Assign each data point to the nearest centroid.
  - d) Recompute the centroids as the mean of the data points assigned to them.
  - e) Repeat steps 3 and 4 until convergence.

The key idea of the method is that the initial centroids are chosen in a way that maximizes the distance between them. By choosing the centroids using a probability distribution which is proportional to the distance between the data points and the nearest centroid, k-means++ selects centroids that are farther apart

from each other, leading to a better initialization and a more accurate clustering. We ran the experiments using four clusters, corresponding to image regions, i.e., background, blood-filled vessel region, external vessel wall and internal vessel wall. The latter region includes pixels belonging to the stenosis. The output of the algorithms is a number of connected components, each with a unique label. The occurrence of a stenosis is detected by identifying more than one blood-filled regions within the vessel, or equivalently, the disconnection of the blood-filled region of the vessel due to the presence of a stenosis.

This method was applied to all simulation and experimental models.

### III. RESULTS AND DISCUSSION

#### A. BIO-ELECTRIC FIELD PERTURBATION BY VESSEL

The perturbation by the subcutaneous vessel of the bio-electric field generated by each electrode tetrapole is evident in the simulation results shown in parts (a) to (c) of Fig. 5. To demonstrate the effect, a side view of the model is used with a single tetrapole placed along the top, in the middle over the skin layer. In line with the tetrapolar impedimetric theory defining the sensitivity distribution [19], i.e. the contribution to the impedance measurement by each point inside the measurand volume, both the injection and the measuring electrode pairs can be shown as generating bio-electric field lines. In Fig. 5(a)-(c) the respective current density fields are shown in red and blue and a vessel vertical to the plane of view is moved from outside the frame to the middle, underneath the tetrapole middle. The field lines are visibly perturbed and this is confirmed in Fig. 5(d) where the resulting impedance generated by the tetrapole for several positions of the vessel from the left to the right of the sensing area results in a symmetrical bell-like curve with the lowest impedance value corresponding to the vessel position shown in Fig. 5(c). Top view snapshots of the isopotential bio-electric field distributions from the four scan sequences on a straight vessel with an orientation of  $-37^\circ$  are shown in Fig. 6, generated by tetrapoles located at the model centre. This indicates both the distribution variability between the scanning orientations, demonstrating the merits of this novel approach, that shows that the tetrapole orientation affects the measurement outcome.

#### B. IMAGE PROCESSING

Fig. 7 illustrates the image processing results from simulation data for each of the four scans of case I, and orientation of  $-37^\circ$ : (a) vertical scan, (b) horizontal scan, (c) and (d) diagonal left and right scans, respectively. It can be seen that the results differ according to the sequence directions. In particular, sequences where the tetrapoles were perpendicular to the blood vessel axis resulted in larger vessel diameter than those featuring tetrapoles parallel to the blood vessel. This suggests that it is not adequate to exclusively rely on the results of a single scanning direction for the study of a

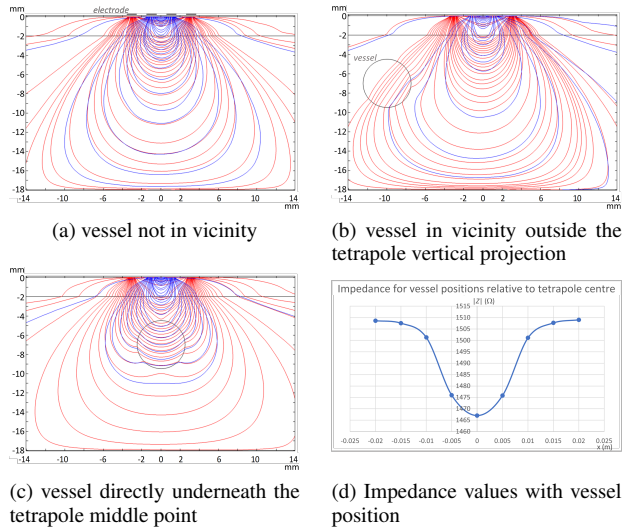


FIGURE 5: Side-view along the tetrapole length of the bio-electric field lines for different relative positions of a subcutaneous vessel. Red field lines correspond to the injecting electrodes and blue ones correspond to the measuring ones. (a) vessel not in vicinity, (b) vessel in vicinity outside the tetrapole vertical projection, (c) vessel directly underneath the tetrapole middle point (d) Impedance values for a range of positions of the vessel, starting from far left to far right.

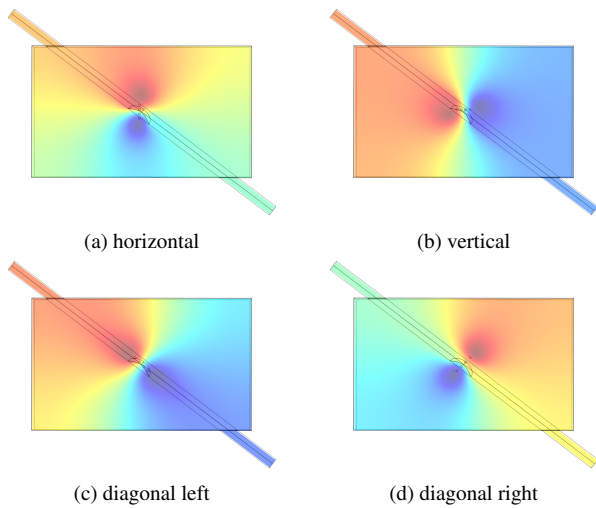


FIGURE 6: Bio-electric field distribution of the model with all four scanning directions, (a) horizontal, (b) vertical, (c) diagonal left and (d) diagonal right, with the tetrapole positioned at the centre of the electrode array.

straight blood vessel. For a bifurcated blood vessel, information obtained from a single scan would not be sufficient for the entire region. The procedure of combining measurements from the four scanning sequence helps eliminate bias due to the geometric relationship between the scanning directions and vessel orientations, as detailed in section II-D. The results of this combination are shown in Fig. 8(a), where after

combining all four scans a single image is formed on which further processing is performed.

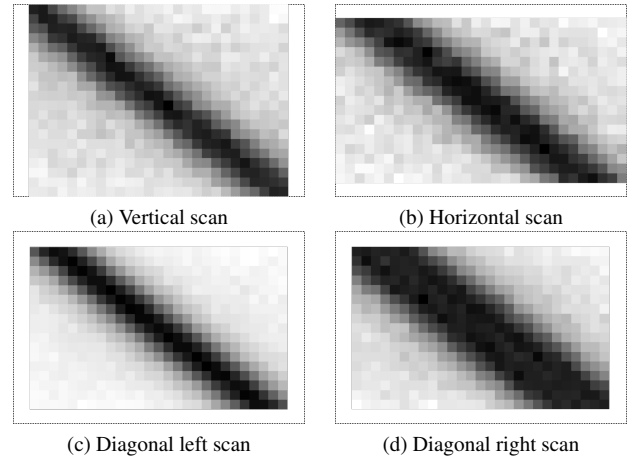


FIGURE 7: Image processing results from simulation data of each of the four scans for case I, and orientation of  $-37^\circ$ : (a) vertical scan (electrodes located at the left and right edges did not contribute). (b) horizontal scan (electrodes located at the top and bottom edges did not contribute). (c) & (d) diagonal scans (electrodes located at the image borders did not contribute).

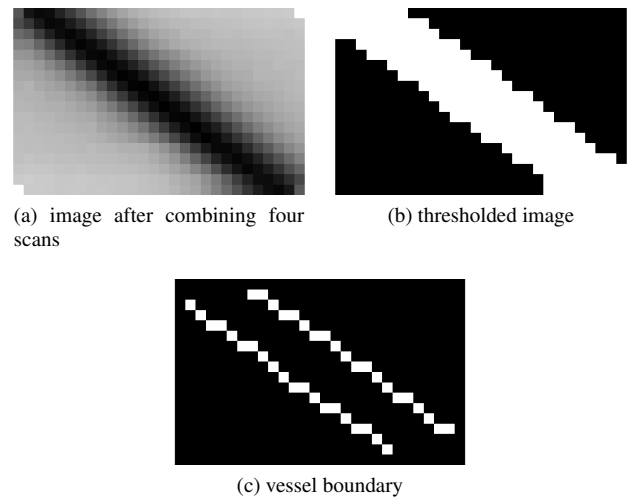


FIGURE 8: Image processing results from simulation data for case I, and orientation of  $-37^\circ$ : (a) Composite image using the measurements of the four scanning directions. (b) Thresholded image. (c) Vessel boundary.

### C. ESTIMATION OF VESSEL ORIENTATION AND EXPERIMENTAL VERIFICATION

To evaluate the proposed method's capability in accurately identifying the orientation of blood vessels with respect to the electrode geometry, blood vessel orientations of  $0^\circ$ ,  $-15^\circ$ ,  $-37^\circ$ ,  $-45^\circ$  and  $-90^\circ$  were simulated. Using the process described in section II-D, measurement data from

the four scan directions for each vessel orientation were combined together with the corresponding 2D bioimpedance map (henceforth referred to as the "composite image") for the orientation of  $-37^\circ$  shown in Fig. 8(a). Thresholding was then applied, indicating the location of the blood vessel relative to the electrode array, as shown in Fig. 8(b). The extracted orientations for simulated vessels at different orientations are given in Table 2. It is also noteworthy that when the vessel orientations are  $0^\circ$ ,  $-45^\circ$  or  $-90^\circ$ , the angles can be estimated with minimal errors. For other angles, the extracted angles are within  $\pm 3^\circ$  of the actual angles.

### 1) Experimental Verification

The detection of a blood vessel with an orientation of  $-37^\circ$  was experimentally verified through measurements on six gelatine phantoms fabricated through the same procedure. The composite image and the resulting detected boundaries of the vessel at the orientation of  $-37^\circ$  in the simulation studies using the smaller model and the electrode sub-array are shown in Fig. 9(a,b). Fig. 9(c,d) show the composite image resulting from the experimental measurements and the resulting extracted boundaries of the vessel at the same orientation. We can observe that the results of the image processing algorithms on both simulated and experimental data are similar. Using the image processing algorithm the extracted angles from the gelatine phantoms resulted to an average value of  $-37.37^\circ \pm 3.09^\circ$ . Thus, it was conclusively demonstrated that the relative orientation of the blood vessel with respect to the electrode array can be identified using the method described in this study. Comparing resolutions from the results of the  $20 \times 30$  and the  $8 \times 16$  arrays it is evident that the minimum number of electrodes used in a potential implementation of the method should be between these two numbers.

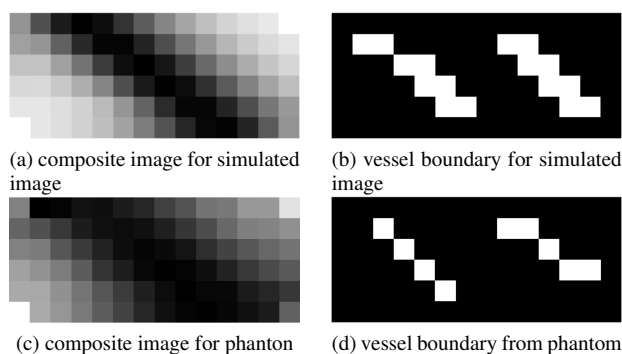


FIGURE 9: Experimental verification: Extraction of vessel boundaries from the experimentally verified  $8 \times 16$  sub-array scans at orientation of  $-37^\circ$ . (a) composite image for simulated vessel. (b) simulated vessel boundary. (c) composite image for gelatine phantom vessel. (d) gelatine phantom vessel boundary.

TABLE 2: Vessel Orientation: Estimated values from the image data vs reference values

Reference Orientation ( $^\circ$ )	Estimated Mean Orientation ( $^\circ$ )	Standard Deviation
0	0	0
-15	-14.77	0.19
-37	-36.1	3.17
-45	-45	0
-90	-90	0

### D. VESSEL FEATURE DETECTION

The procedure described in II-D for case III resulted in the images shown in Fig. 10 for the bifurcated vessel. Fig. 10(a) shows the composite image for case III without the presence of stenosis. Applying thresholding to this image results to Fig. 10(b), while the vessel edges are shown in Fig. 10(c). As it can be seen, increasing the size of the electrode array results in better identification of the bifurcation. This shows that, with a sufficient number of electrodes, straight vessels, as well as vessels with bifurcations, can be identified using the method described in this work.

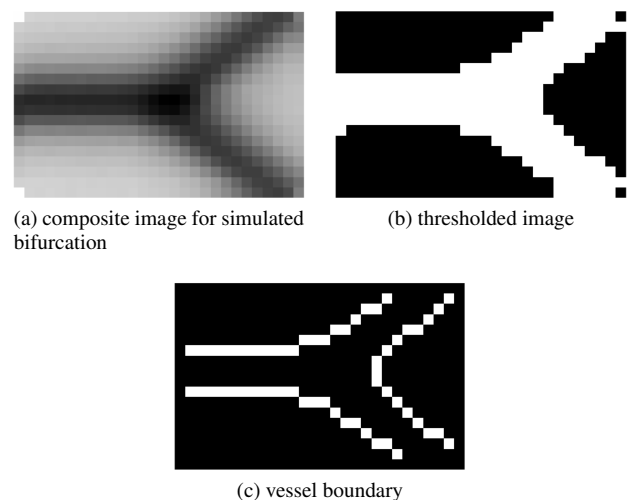


FIGURE 10: Image processing results from the simulation data of case III and orientation of  $0^\circ$  for the straight part of the vessel structure (no stenosis present): (a) Composite image using the simulation results of the four scanning directions, (b) Thresholded image, (c) Vessel boundary.

### E. DETECTION OF STENOSIS

The detection of stenosis was studied for two cases, i.e., case II (stenosis in a straight vessel) and case IV (stenosis in a vessel with bifurcation).

#### 1) Straight Vessel with Stenosis

The results for the straight-line vessel with the presence of stenosis, obtained from the simulations were processed using the procedure described in section II-D to evaluate the ability of the proposed method in detecting the occurrence

of stenosis. A number of stenosis scenarios were considered, specifically, 0 % (no stenosis), 20 %, 40 %, 60 % and 80 %. Fig. 11(a) shows the image obtained after processing, with the slightly lighter grey area within the vessel boundary indicating the stenosis region, for the reference value of 40 %. The estimated stenosis area (shown in Fig. 11(b)) was obtained by following the method described in section II-D, step 'g'. Table 3 provides stenosis detection accuracies for different levels of stenoses in the case of straight vessels, and shows that stenoses can be detected with accuracy of 97.78%. The results demonstrate that stenosis detection accuracy drops to 88.89% in the case of low degree stenosis (defined as less than 40%), specifically, at 20%. A possible reason for this is the limited size of the composite image, which impacts on the accurate determination of the size of the stenosis region.

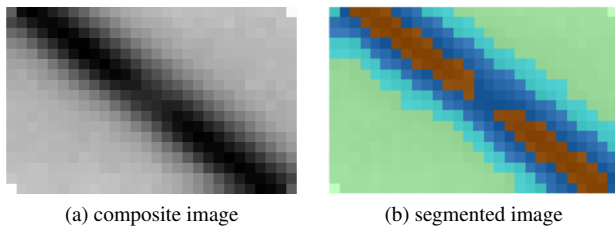


FIGURE 11: Image processing results for case II at an orientation of  $-37^\circ$  and reference stenosis percentage of 40% (simulation data): (a) composite image (stenosis barely visible as slightly lighter grey inside the vessel boundaries), (b) segmented image showing background, inner/outer vessel boundaries and blood filled region. The stenosis area is clearly visible with the same colouration as the inner vessel boundary.

TABLE 3: Accuracy of stenosis detection in a straight line vessel (out of 9 scans)

Stenosis %	Detection Accuracy %
0	100
20	88.89
40	100
60	100
80	100
<b>Average</b>	<b>97.78</b>

TABLE 4: Accuracy of stenosis detection in a bifurcated vessel (out of 9 scans)

Stenosis %	Detection Accuracy %
0	100
20	66.67
40	88.89
60	100
80	100
<b>Average</b>	<b>91.11</b>

## 2) Vessel with Bifurcation and Stenosis

The simulations for a bifurcated vessel with stenosis were carried out as in the previous section. The resulting composite image is shown in 12(a) and the boundary of the bifurcated vessel and its stenosis can be seen in Fig. 12(b). Table 4 provides stenosis detection accuracies for different levels of stenoses in the case of bifurcated vessels, and shows that stenoses can be detected with an average accuracy of 91.11%. As in the previous case, the results demonstrate that stenosis detection accuracy drops to 66.67% and 88.89% in the case of 20% and 40% stenoses, respectively, i.e., low degree stenosis.

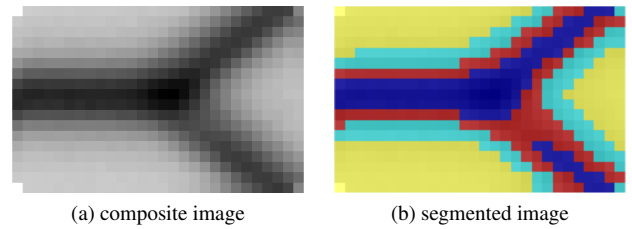


FIGURE 12: Image processing results for case IV for a bifurcated vessel with orientation of  $0^\circ$  and reference stenosis percentage of 20% (simulation data): (a) composite image (stenosis barely visible as slightly lighter grey inside the vessel boundaries), (b) segmented image showing background, inner/outer vessel boundaries and blood filled region. The stenosis area is clearly visible with the same colouration as the inner vessel boundary.

## IV. CONCLUSIONS

In this work, a new planar bioimpedance mapping method was presented, which is based on a fourfold scanning procedure using a planar electrode array. The contributions of the method, especially in relation to conventional EIT, included: the fact that the impedimetric sensor is planar, rather than encompassing the targeted biology, thus providing more flexibility for accessing superficial biological features; the tetrapole geometry being kept constant throughout the scanning process, thus requiring no inter-measurement weighting; and the quad-directional scanning. The latter offers three advantages, namely higher spatial resolution offered by the combined results of the four scans; less dependency on the tetrapole shape (here rectangular); and less dependency on the blood vessel's orientation. The proposed approach was studied through FEM simulations using a simplified biological model consisting of skin and fat layers and blood vessels with and without bifurcations and stenoses. The model did not include more complex biological features like neighbouring vasculature or muscle tissue, which are the next logical step for further research. Similar to a plethora of FEM based research simplified models are very appropriate for demonstrating a proof-of-concept assessment of a new method. Experimental verification was carried out for one of the cases examined through the use of a multi-layered gelatine vascular

phantom. Using image processing methods, the results obtained demonstrate that this method is able to provide good quality impedance information on blood vessel location and orientation. The precise positioning of electrodes is critical for reliable measurements, and any inaccuracies in placement could impact the effectiveness of the sensing method; however, the proposed method reduces the need for precise placement to some extent. Practical implications of our proposed method in clinical applications will require further detailed analysis of the sensor array. Although valuable for a range of clinical applications, the sensors placed on the skin present some clinical challenges, encompassing issues like accurate electrode placement, skin variability, including differences in thickness and composition among individuals, motion artefacts can introduce noise, which is crucial for reliable data control in clinical settings, Patient-specific factors like hydration status, body composition, and skin conditions influence bioimpedance measurements, requiring tailored calibration and interpretation. The problems that could arise during clinical applications are beyond the proof-of-concept stage and can be addressed in future studies. The results of each of the four scans individually also demonstrated that the orientation of the tetrapole in electrical impedance imaging (e.g., in EIT) plays a role in the quality of the outcome. Beyond its potential low cost, the proposed system does not require specialist training to be operated, e.g., to ensure exact and well-aligned sensor placement over the targeted vasculature as in other methods. Most importantly, information was extracted regarding vascular features, such as bifurcations and stenoses, demonstrating the ability not only to detect features but to accurately detect the presence of stenosis even when it is of a low grade. Given the large amount of undetected carotid atherosclerosis cases that lead to debilitating or even fatal strokes, the findings of this study are significant as they can lead to a low-cost diagnostic method for early screening medical examinations. Such screening examinations could be practised in primary care or at remote clinics - possibly even at home - providing a warning even without the presence of any symptoms, thus allowing for the referral of patients for further in-depth examinations when needed.

## REFERENCES

- [1] J. Park, A. Razuk, P. Saad, G. Telles, W. Karakhanian, A. Fioranelli, A. Rodrigues, G. Volpiani, P. Campos, R. Yamada, V. Castelli, and R. Caffaro, "Carotid stenosis: what is the high-risk population?," *Clinics*, vol. 67, pp. 865–870, 8 2012.
- [2] M. de Weerd, J. P. Greving, B. Hedblad, M. W. Lorenz, E. B. Mathiesen, D. H. O'Leary, M. Rosvall, M. Sitzer, G. J. de Borst, E. Buskens, and M. L. Bots, "Prediction of Asymptomatic Carotid Artery Stenosis in the General Population," *Stroke*, vol. 45, no. 8, pp. 2366–2371, 2014.
- [3] E. M. Tuzcu, S. R. Kapadia, E. Tutar, K. M. Ziada, R. E. Hobbs, P. M. McCarthy, J. B. Young, and S. E. Nissen, "High Prevalence of Coronary Atherosclerosis in Asymptomatic Teenagers and Young Adults : Evidence From Intravascular Ultrasound," *Circulation*, vol. 103, no. 22, pp. 2705–2710, 2001.
- [4] E. G. Grant, C. B. Benson, G. L. Moneta, A. V. Alexandrov, J. D. Baker, E. I. Bluth, B. A. Carroll, M. Eliasziw, J. Gocke, B. S. Hertzberg, S. Katarick, L. Needleman, J. Pellerito, J. F. Polak, K. S. Rholl, D. L. Wooster, and E. Zierler, "Carotid artery stenosis: grayscale and Doppler ultrasound diagnosis—Society of Radiologists in Ultrasound consensus conference," in *Ultrasound quarterly*, vol. 19, pp. 190–198, Lippincott Williams & Wilkins, 2003.
- [5] P. R. Hoskins, K. Martin, and A. Thrush, *Diagnostic Ultrasound Physics and Equipment*. Cambridge: Cambridge University Press, 2 ed., 2010.
- [6] M. M. Horrow, J. Stassi, A. Shurman, J. D. Brody, C. L. Kirby, and H. K. Rosenberg, "The limitations of carotid sonography: Interpretive and technology-related errors," *American Journal of Roentgenology*, vol. 174, no. 1, pp. 189–194, 2000.
- [7] M. Takhti and K. Odame, "A Power Adaptive, 1.22-pW/Hz, 10-MHz Read-Out Front-End for Bio-Impedance Measurement," *IEEE Transactions on Biomedical Circuits and Systems*, vol. 13, pp. 725–734, 8 2019.
- [8] R. Matera and S. Ricci, "Automatic measurement of the carotid blood flow for wearable sensors: A pilot study," *Sensors*, vol. 21, no. 17, p. 5877, 2021.
- [9] J.-É. S. Kenny, C. E. Munding, J. K. Eibl, A. M. Eibl, B. F. Long, A. Boyes, J. Yin, P. Verrecchia, M. Parrotta, R. Gatzke, et al., "A novel, hands-free ultrasound patch for continuous monitoring of quantitative doppler in the carotid artery," *Scientific Reports*, vol. 11, no. 1, pp. 1–11, 2021.
- [10] B. D. Nenova, I. T. Iliev, and A. Photoplethysmography, "Non-Invasive Methods of Peripheral Pulse Detection : Advantages and Disadvantages," *Annual Journal of Electronics*, pp. 57–60, 2009.
- [11] A. Ikarashi, M. Nogawa, T. Yamakoshi, S. Tanaka, and K. I. Yamakoshi, "An optimal spot-electrodes array for electrical impedance cardiography through determination of impedance mapping of a regional area along the medial line on the thorax," *Annual International Conference of the IEEE Engineering in Medicine and Biology - Proceedings*, pp. 3202–3205, 2006.
- [12] M. Qu, Y. Zhang, J. G. Webster, and W. J. Tompkins, "Motion Artifact from Spot and Band Electrodes During Impedance Cardiography," *IEEE Transactions on Biomedical Engineering*, vol. BME-33, no. 11, pp. 1029–1036, 1986.
- [13] Z. Q. Hashim, L. Constantinou, and I. F. Triantis, "Modelling Dynamically Re-Sizeable Electrodes (DRE) for Targeted Transcutaneous Measurements in Impedance Plethysmography," *IEEE Transactions on Biomedical Circuits and Systems*, vol. 14, pp. 104–112, 2 2020.
- [14] M. Stankiewicz-Rudnicki, T. Gaszyński, and W. Gaszyński, "Assessment of regional ventilation in acute respiratory distress syndrome by electrical impedance tomography," *Anaesthesiology Intensive Therapy*, vol. 47, no. 1, pp. 77–81, 2015.
- [15] J. Bordes, P. Goutorbe, P. J. Cungi, M. C. Boghossian, and E. Kaiser, "Noninvasive ventilation during spontaneous breathing anesthesia: An observational study using electrical impedance tomography," *Journal of Clinical Anesthesia*, vol. 34, pp. 420–426, 2016.
- [16] R. Bayford, "Bioimpedance Tomography (Electrical Impedance Tomography)," *Annual Review of Biomedical Engineering*, vol. 8, no. 1, pp. 63–91, 2006.
- [17] S. a. Weber, N. Watermann, J. Jossinet, J. A. Byrne, J. Chantrey, S. Alam, K. So, J. Bush, S. O' Kane, and E. T. McAdams, "Remote wound monitoring of chronic ulcers," *IEEE Transactions on Information Technology in Biomedicine*, vol. 14, no. 2, pp. 371–377, 2010.
- [18] B. Brown, "Electrical impedance tomography (EIT): a review," *Journal of Medical Engineering & Technology*, vol. 27, no. 3, pp. 97–108, 2003.
- [19] S. Grimnes and Ø. G. Martinsen, *Bioimpedance and Bioelectricity Basics*. Elsevier, 2015.
- [20] D. Naranjo-Hernández, J. Reina-Tosina, and M. Min, "Fundamentals, recent advances, and future challenges in bioimpedance devices for healthcare applications," *Journal of Sensors*, vol. 2019, 2019.
- [21] Y. H. Shash, M. A. A. Eldosoky, and M. T. Elwakad, "The effect of vascular diseases on bioimpedance measurements: mathematical modeling," *Biomedical Research and Therapy*, vol. 5, pp. 2414–2431, 6 2018.
- [22] D. S. Holder, *Electrical Impedance Tomography: Methods, History and Applications*. CRC Press, 2004.
- [23] E. Teschner, M. Imhoff, and S. Leonhardt, "Electrical Impedance Tomography: The realisation of regional ventilation monitoring 2nd edition," *Drager*, vol. 1, pp. 81–87, 9 2010.
- [24] F. Lu, C. Wang, R. Zhao, L. Du, Z. Fang, X. Guo, and Z. Zhao, "Review of stratum corneum impedance measurement in non-invasive penetration application," *Biosensors*, vol. 8, no. 2, 2018.
- [25] Z. Q. Hashim, L. Constantinou, P. A. Kyriacou, and I. F. Triantis, "A novel approach to transcutaneous localization of blood vessels using a dynamically reconfigurable electrode (DRE) array," in *2016 IEEE Biomedical Circuits and Systems Conference (BioCAS)*, vol. 44, pp. 424–427, IEEE, 10 2016.

[26] L. Rems, "Applicative use of electroporation models: From the molecular to the tissue level," in *Advances in Biomembranes and Lipid Self-Assembly*, vol. 26, pp. 1–50, Elsevier, 2017.

[27] K. Sel, N. Huerta, M. S. Sacks, and R. Jafari, "Parametric modeling of human wrist for bioimpedance-based physiological sensing," in *ICASSP 2022-2022 IEEE International Conference on Acoustics, Speech and Signal Processing (ICASSP)*, pp. 1161–1165, IEEE, 2022.

[28] O. Akouissi, S. P. Lacour, S. Micera, and A. DeSimone, "A finite element model of the mechanical interactions between peripheral nerves and intrafascicular implants," *Journal of Neural Engineering*, vol. 19, no. 4, p. 046017, 2022.

[29] S. Standring, *Gray's Anatomy, The Anatomical Basis of Clinical Practice, Expert Consult*, 40th Edition. Elsevier, 2008.

[30] K. Van de Graaff, R. W. Rhees, and S. L. Palmer, *Schaum's Outline of Human Anatomy and Physiology, Third Edition (Schaum's Outline Series)*. Schaum's Outline Series, 2009.

[31] L. J. Liao, W. C. Lo, W. L. Hsu, P. W. Cheng, and C. P. Wang, "Assessment of pain score and specimen adequacy for ultrasound-guided fine-needle aspiration biopsy of thyroid nodules," *Journal of Pain Research*, vol. 11, pp. 61–66, 2018.

[32] F.-J. Pettersen and J. O. Høgetveit, "From 3D tissue data to impedance using Simpleware ScanFE+IP and COMSOL Multiphysics – a tutorial," *Journal of Electrical Bioimpedance*, vol. 2, no. 1, pp. 13–32, 2011.

[33] C. Gabriel, S. Gabriel, and E. Corthout, "The dielectric properties of biological tissues: {I. Literature} survey," *Physics in medicine and biology*, vol. 41, no. 11, p. 2231, 1996.

[34] S. Gabriel, R. W. Lau, and C. Gabriel, "The dielectric properties of biological tissues: III. Parametric models for the dielectric spectrum of tissues," *Physics in Medicine and Biology*, vol. 41, pp. 2271–2293, 11 1996.

[35] C. L. Higgins, S. A. Marvel, and J. D. Morrisett, "Quantification of calcification in atherosclerotic lesions," *Arteriosclerosis, Thrombosis, and Vascular Biology*, vol. 25, no. 8, pp. 1567–1576, 2005.

[36] J. P. Gittings, C. R. Bowen, A. C. Dent, I. G. Turner, F. R. Baxter, and J. B. Chaudhuri, "Electrical characterization of hydroxyapatite-based bioceramics," *Acta Biomaterialia*, vol. 5, no. 2, pp. 743–754, 2009.

[37] P. Kassanos, A. Demosthenous, and R. H. Bayford, "Towards an optimized design for tetrapolar affinity-based impedimetric immunosensors for lab-on-a-chip applications," in *2008 IEEE Biomedical Circuits and Systems Conference*, pp. 141–144, IEEE, 2008.

[38] O. G. Martinsen and S. Grimnes, *Bioimpedance and bioelectricity basics*. Academic press, 2011.

[39] X. Liu, A. Demosthenous, and N. Donaldson, "Platinum electrode noise in the eng spectrum," *Medical & biological engineering & computing*, vol. 46, no. 10, pp. 997–1003, 2008.

[40] V. Chitturi and N. Farrukh, "Spatial resolution in electrical impedance tomography: A topical review," *Journal of Electrical Bioimpedance*, vol. 8, no. 1, pp. 66–78, 2017.

[41] A. T. Mobashsher and A. M. Abbosh, "Artificial human phantoms: Human proxy in testing microwave apparatuses that have electromagnetic interaction with the human body," *IEEE Microwave Magazine*, vol. 16, no. 6, pp. 42–62, 2015.

[42] D. Bennett, "NaCl doping and the conductivity of agar phantoms," *Materials Science and Engineering C*, vol. 31, no. 2, pp. 494–498, 2011.

[43] T. J. Kao, G. J. Saulnier, D. Isaacson, T. L. Szabo, and J. C. Newell, "A versatile high-permittivity phantom for EIT," *IEEE Transactions on Biomedical Engineering*, vol. 55, no. 11, pp. 2601–2607, 2008.

[44] N. Otsu, "A Threshold Selection Method from Gray-Level Histograms," *IEEE Transactions on Systems, Man, and Cybernetics*, vol. 9, pp. 62–66, 1 1979.

[45] J. Yang and X. Li, "Boundary detection using mathematical morphology," *Pattern Recognition Letters*, vol. 16, no. 12, pp. 1277–1286, 1995.

[46] R. Gonzalez and R. Woods, *Digital Image Processing*. Pearson, 4th ed., 2017.

[47] D. Arthur and S. Vassilvitskii, "K-means++: The advantages of careful seeding," in *Proceedings of the Annual ACM-SIAM Symposium on Discrete Algorithms*, 2007.



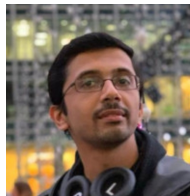
ENAYETUR RAHMAN received his BSc in Electrical and Electronic Engineering degree from Bangladesh University of Engineering and Technology in 2003 and PhD in Photonics from City, University of London in 2015. He joined the Department of Computer Science and Engineering, Darul Ihsan University, Bangladesh as a Lecturer. He later joined United International University, Bangladesh as a Senior Lecturer in the Department of Electrical and Electronic Engineering in 2006.

From 2015 to 2017, he worked in the Research Centre for Biomedical Engineering, City, University London as a Research Associate. He worked in the Biodevices Laboratory within the Nanotechnology and Integrated Bioengineering Centre (NIBEC), School of Engineering, Ulster University from 2018 to 2022 as Research Associate. He has been working in the Research Centre for Biomedical Engineering, City, University London as a Senior Research Associate since 2022. His main areas of research interest are Impedance Spectroscopy, Photonics, Light-Biological matter interaction, NIR spectroscopy, Computational Modelling, Non-invasive detection, and Machine Learning.



PANOS LIATIS (SMIEEE) received the Diploma degree in electrical engineering from the University of Thrace, Greece, and the Ph.D. degree in electrical engineering and electronics from the University of Manchester, U.K. He is currently a Professor with the Department of Electrical Engineering and Computer Science, Khalifa University of Science and Technology. He commenced his academic career at the University of Manchester, prior to joining City, University of

London, U.K., where he was a Professor and the Head of the Electrical and Electronic Engineering Department. His research interests are image processing, computer vision, pattern recognition, and machine learning.



ZAHEER Q. HASHIM (S '16) was born in Kuwait, in 1987. He received the B.Eng. degree in electronic engineering from UEL, London, U.K., in 2012, the M.Sc in computer systems engineering from UEL, London, U.K., and Ph.D. degree in bio-medical engineering at City, University of London, U.K. His research interests are in the area of micro-controller based programming, instrumentation and sensors for biointerfacing research.



PANAYIOTIS A. KYRIACO (SMIEEE) is a Professor of Biomedical Engineering at City, University of London, where he founded the Biomedical Engineering Research Centre. His research focuses on utilizing Photoplethysmography (PPG) for non-invasive optical sensor technologies to diagnose diseases and monitor health and fitness. Prof. Kyriacou has authored over 300 publications and holds six patents in medical optical sensors. He has served in leadership positions at the Institute of Physics and Engineering in Medicine (IPEM), UK and as President of the European Alliance for Medical and Biological Engineering and Science.

Prof. Kyriacou is a Fellow of IoP, IPEM and IET and Senior Member of IEEE. He also serves as a consultant for medical device industries.



IASONAS F. TRIANTIS (M '01 – SM '20) was born in Geneva, Switzerland in 1976. He received his MEng in Electronic Engineering from the University of Manchester Institute of Science and Technology (UMIST) in 2000 and his PhD in Medical Electronics from University College London (UCL) in 2005. He was a Senior Research Associate on Electrical Impedance Tomography at UCL between 2010-12; a Research Associate in Neuroprostheses at Imperial College London

between 2005-10; and a Research Assistant in Implantable Devices at UCL between 2000 -05. He is currently a Senior Lecturer in Biomedical Engineering with a research interest on medical devices focusing on electroceuticals for neural engineering and bioimpedance sensing. His research encompasses the development of targeted diagnostic and therapeutic technology; new sensing methods for point-of-care diagnostics; and empowering patients by improving therapy management. He has worked on technology aimed at spinal cord injury, vagus nerve stimulation, lung and bowel cancer imaging, mental health therapy management, peripheral vascular disease, and wound healing.

...